

Vibration analysis of rotating variable-angle-tow composite cylindrical structures via high-fidelity shell models

Original

Vibration analysis of rotating variable-angle-tow composite cylindrical structures via high-fidelity shell models / Azzara, Rodolfo; Filippi, Matteo; Carrera, Erasmo. - In: THIN-WALLED STRUCTURES. - ISSN 0263-8231. - 205:Part A(2024). [10.1016/j.tws.2024.112446]

Availability:

This version is available at: 11583/2992970 since: 2024-10-01T11:50:47Z

Publisher:

Elsevier

Published

DOI:10.1016/j.tws.2024.112446

Terms of use:

This article is made available under terms and conditions as specified in the corresponding bibliographic description in the repository

Publisher copyright

(Article begins on next page)



Full length article

Vibration analysis of rotating variable-angle-tow composite cylindrical structures via high-fidelity shell models

R. Azzara^{*,1}, M. Filippi¹, E. Carrera²^{MUL²}, Lab, Department of Mechanical and Aerospace Engineering, Politecnico di Torino, Corso Duca degli Abruzzi 24, 10129 Torino, Italy

ARTICLE INFO

Keywords:

Finite element method
Carrera Unified Formulation
High-order shell models
Variable-angle-tow
Composite
Cylinders

ABSTRACT

The paper focuses on rotordynamics analyses of various rotating variable-angle-tow (VAT) composite cylindrical structures using both low- and high-fidelity structural models. To model the spatially varying composite shell structures, the Carrera Unified Formulation (CUF) is employed. The CUF provides a hierarchical and automated approach for developing shell finite element models. Various shell models are created using different kinematics models based on Taylor or Lagrange expansion functions. The linearized equations of motion include the Coriolis and initial stress contributions. Several VAT composite curved panels and thin and thick cylinders have been analyzed to validate the presented approach and provide benchmark solutions. The results are discussed and compared with commercial software solutions. The results demonstrate the good accuracy and reliability of the proposed numerical methodology.

1. Introduction

Cylindrical shell structures have gained significant attention in the industrial sector due to their advantageous strength-to-weight ratio and manufacturing convenience. They have emerged as essential components in various machines, including jet engines, centrifugal separators, rockets, missiles, offshore drilling systems, and spinning satellite structures. During operation, these structures are subjected to several dynamic forces that can affect their integrity and the efficiency of the equipment they support. Consequently, performing comprehensive vibrational analysis on these structures is crucial for their design and performance assessment.

The existing shell theories widely used today are based on linear elasticity principles and classical shell theory (CST). The pioneering work in this field was carried out by Love [1], who introduced a successful thin shell theory based on classical linear elasticity. Subsequently, Donnell [2], Sanders [3], and Leissa [4] incorporated their assumptions into linear elasticity shell theories, deriving different equations of motion that exhibited improved accuracy in predicting shell structure behaviors. To overcome the limitations of the classical theory, Reissner [5] and Mindlin [6] introduced the First-order Shear Deformation Theory (FSDT). Over time, various high-order two-dimensional (2D) theories have been developed to overcome the limitations of classical studies' assumptions. For instance, Reddy [7] introduced a refined approach that incorporates through-the-thickness kinematics

and considers high-order shear deformations. This theory has been particularly useful in analyzing 2D composite structures. Carrera [8] unified the refined theories of shell models in his work.

The investigation of dynamic analysis of rotating cylindrical shells has a rich history spanning approximately a century. Bryan [9] was the pioneering researcher who studied rotating cylindrical shells, specifically focusing on a rotating ring. In his work, he observed the occurrence of traveling modes for the first time. Building upon this research, DiTaranto and Lessen [10] further advanced the research by considering the Coriolis effect in their analysis of rotating shells. Padovan [11] investigated the natural frequencies of rotating pre-stressed cylindrical structures using a thin shell theory. An exact solution for free vibration analyses of thin rotating composite cylindrical shells was presented by Rand and Stavsky [12]. High-speed rotating shells were analyzed by Chen et al. [13] by adopting the Novoshilov theory. Loveday and Rogers [14] conducted various free vibration analyses of elastically supported thin rotating cylindrical shells, accounting for the gyroscopic effect with the Flogged shell theory. Spinning laminated composite cylindrical shells were investigated by Lam and Loy [15]. They derived a quadratic order equation that describes the frequencies of infinitely long rotating laminated cylinders. Lee and Kim [16] conducted vibration analyses of orthogonally stiffened composite cylinders under rotation. Zhao et al. [17] studied the free vibration characteristics of laminated composite rotating cylinders under various conditions,

* Corresponding author.

E-mail addresses: rodolfo.azzara@polito.it (R. Azzara), matteo.filippi@polito.it (M. Filippi), erasmo.carrera@polito.it (E. Carrera).¹ Assistant Professor.² Professor of Aerospace Structures and Aeroelasticity.

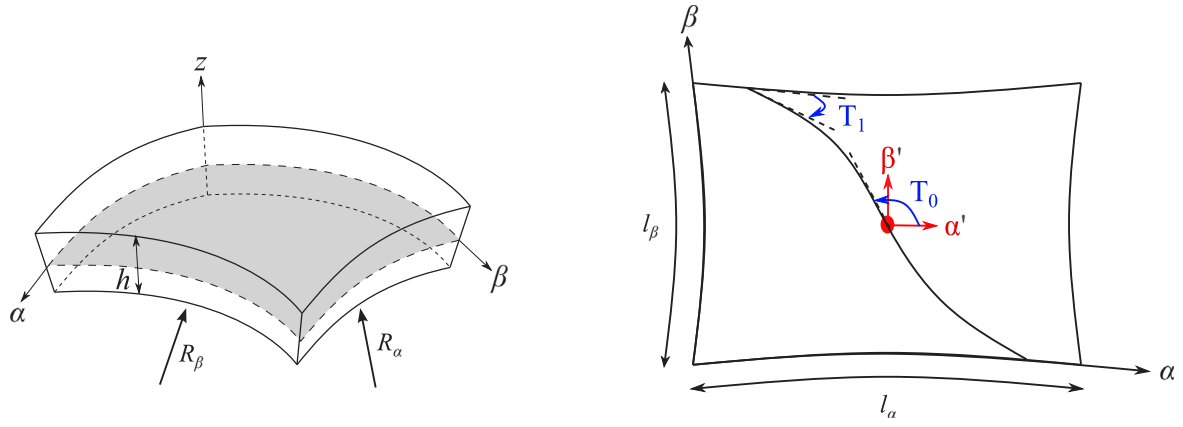


Fig. 1. Representative VAT composite shell model.

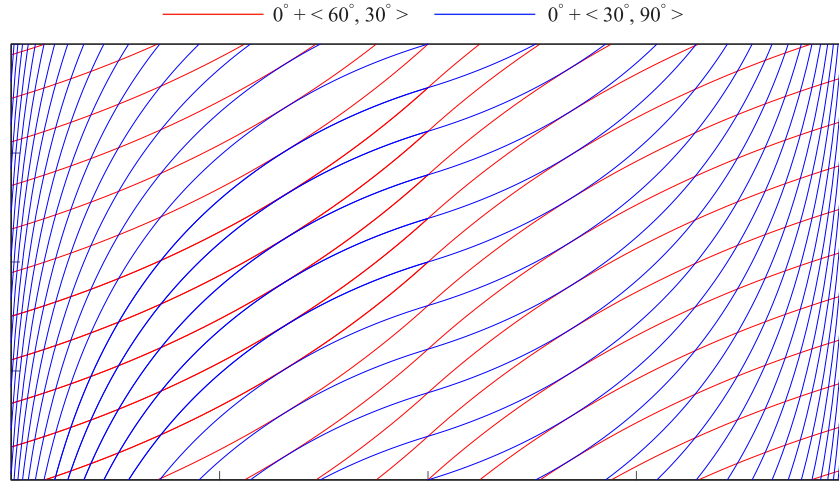


Fig. 2. Graphical representation of spatially varying fibers path over a representative domain.

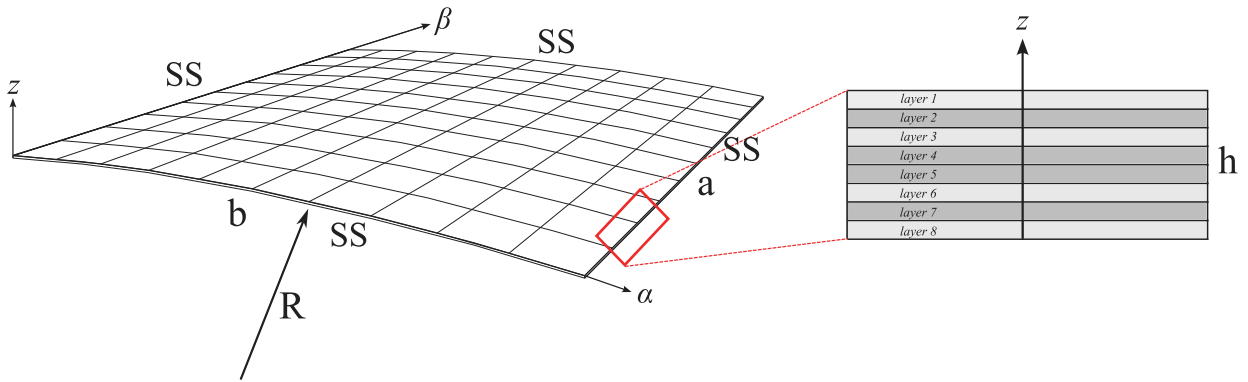


Fig. 3. Geometry, boundary conditions and mesh discretization of the curved panel.

using the Ritz method and considering the presence of added stringer and ring stiffeners. Sivadas [18] performed vibration analyses of prestressed rotating thick conical shell structures, investigating the effect of shear deformation and material damping on frequencies and damping factors. Guo et al. [19] investigated the influence of rotation on the vibrations of thick cylindrical shell structures by employing a non-linear plate-shell theory. More recently, Filippi et al. [20] conducted rotordynamic analyses of cylindrical models using high-order 2D shell models based on the Carrera Unified Formulation (CUF), including both Coriolis and spin-softening contributions. Azzara et al. [21] proposed a novel approach for rotordynamic analyses of stiffened cylinders and

disks, adopting high-fidelity shell models with three-dimensional (3D) capabilities.

Advancements in automated manufacturing processes have revolutionized the use of composite materials, leading to the development of innovative techniques that offer improved repeatability, higher production rates, and fewer defects in composite structures. Automation provides the added benefit of fiber steering, providing designers greater flexibility in customizing the characteristics of composites compared to conventional straight fiber reinforcements. By tailoring the fiber path in different layers, the vibration performance of structures can be further improved. One technique that enables the fabrication of

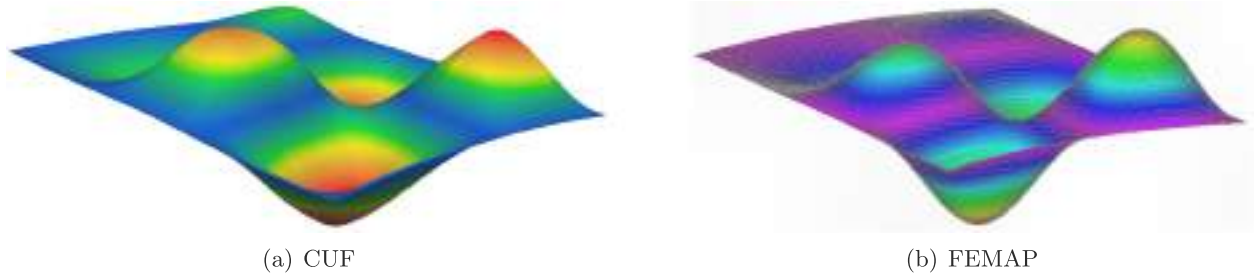


Fig. 4. Comparison of the first buckling mode shape of the VAT composite curved panel $[0^\circ \pm (0^\circ/30^\circ)]_{2s}$.

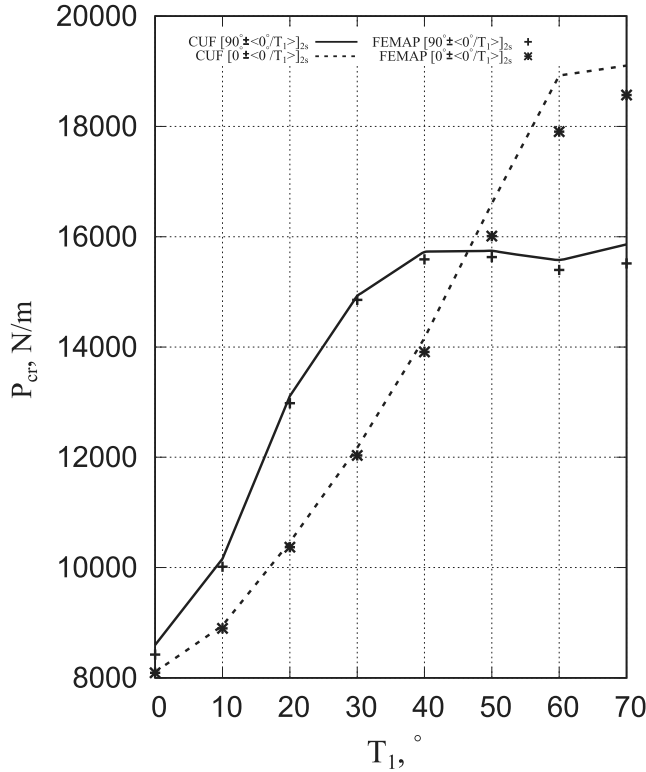


Fig. 5. Variation of the first buckling load with respect to the T_1 parameter. VAT composite curved panel subjected to in-plane compressive loads.

variable-angle-tow (VAT) composites involves curvilinear steering of the fiber tow paths within the lamina plane. This approach allows for variations in stiffness distribution, leading to load redistribution in critical regions of the structure. Manufacturing methods, such as automated fiber placement (AFP), automated tape laying (ATL), and continuous tow shearing (CTS), are employed to produce VAT composites, as documented in studies by Kim et al. [22] and Dirk et al. [23], among others. Pioneering research conducted by Hyer and Lee [24] explored the effects of curvilinear fibers around a cutout in a flat composite plate. Further numerical studies by Hyer and Charette [25] and by Schueler and Hale [26] provided additional evidence of the advantages offered by curvilinear fibers. Tatting and Gurdal [27] demonstrated significant improvements in strength, stiffness, and buckling load through their experimental study on the development, production, and evaluation of flat variable stiffness plates. Other researchers, such as Peeters and Abdalla [28], Van Campen et al. [29], and White et al. [30], have also contributed to the understanding of flat tow-steered laminated plate structures. Accurate stress analyses of VAT shell structures via variable-fidelity models were provided in [31].

While numerous studies have focused on variable stiffness plates, only a minority have centered their attention on VAT cylindrical shells. For example, Tatting [32] investigated variations in circumferential stiffness on cylindrical shells. Wu [33] utilized advanced fiber placement technology to circumferentially tailor the stiffness of cylinders in bending. White and Weaver [34] employed optimized variable-angle-tow techniques in the lamination of cylindrical shells to mitigate the sensitivity of these structures to geometric imperfections. Blom et al. [35] examined the maximization of fundamental frequency of conical shells with variable stiffness, finding that VAT laminates could enhance the fundamental frequency compared to laminates with straight fiber paths, even considering manufacturing limitations. The dynamic behavior of doubly-curved panels reinforced by curvilinear fibers was presented by Tornabene et al. [36].

The existing literature on the natural frequencies of rotating structures primarily focuses on isotropic or classical composite structures, with a gap in research regarding VAT composite cylindrical structures. To address this research gap, this paper aims to introduce various rotordynamics analyses of VAT shell structures. The primary goal of this work is to accurately predict the dynamic response of rotating tow-steered composite shells and provide vibration benchmarks for future evaluations.

The proposed methodology relies on the Carrera Unified Formulation (CUF) [37]. This formulation allows for the straightforward adoption of classical to high-order models by expressing any theory as generalized kinematics through the expansion of generalized variables. By employing this approach, the governing equations and the corresponding finite element (FE) arrays of 2D theories are expressed in terms of Fundamental Nuclei (FNs), which represent the main building blocks of the presented methodology. In this research, the formulation is specifically applied to address rotordynamics analyses of shell structures, taking into account all effects stemming from rotation, such as the Coriolis force, centrifugal force, spin-softening matrix, and stress-stiffening matrix. For subsequent analyses of rotating thin and thick cylinders, a linearized approach has been employed.

This article is organized as follows: (i) Section 2 provides the rotordynamics equations in CUF formalism, including a description of the VAT technique; (ii) then, Section 3 presents various numerical results and (iii) finally, some conclusions are drawn in Section 4.

2. Vibrations of rotating VAT shells

2.1. Preliminaries

A shell geometry is described employing an orthogonal curvilinear reference system $(\alpha; \beta; z)$, as reported in Fig. 1, where $\alpha - \beta$ indicates the in-plane surface and z the thickness direction. The displacement, strain and stress fields for each layer k are expressed as follows:

$$\begin{aligned} \mathbf{u}^k &= \{u_\alpha^k, u_\beta^k, u_z^k\}^T \\ \boldsymbol{\epsilon}^k &= \{\epsilon_{\alpha\alpha}^k, \epsilon_{\beta\beta}^k, \epsilon_{zz}^k, \epsilon_{\alpha z}^k, \epsilon_{\beta z}^k, \epsilon_{\alpha\beta}^k\}^T \\ \boldsymbol{\sigma}^k &= \{\sigma_{\alpha\alpha}^k, \sigma_{\beta\beta}^k, \sigma_{zz}^k, \sigma_{\alpha z}^k, \sigma_{\beta z}^k, \sigma_{\alpha\beta}^k\}^T \end{aligned} \quad (1)$$

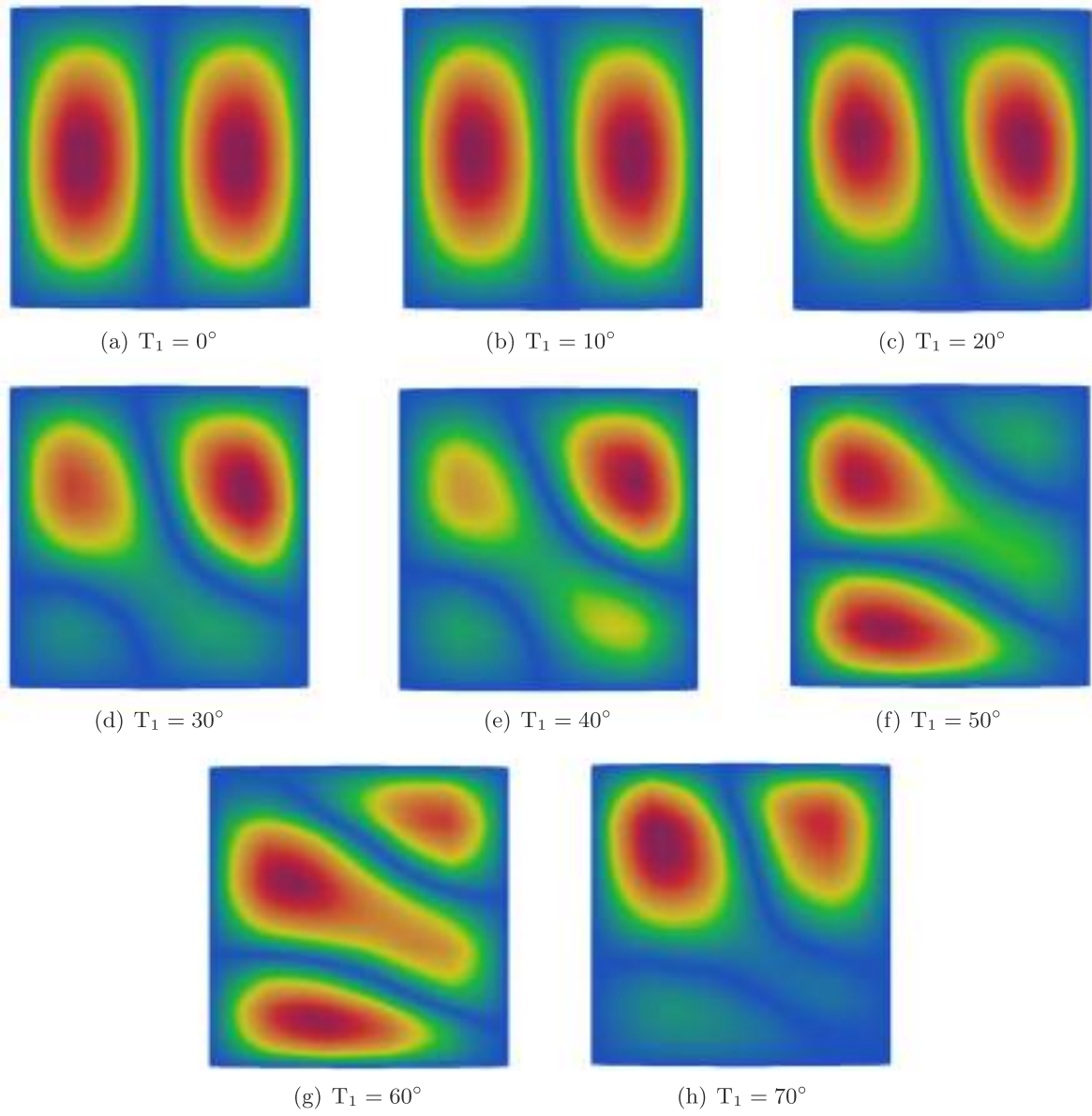


Fig. 6. First buckling mode shape with respect to the T_1 parameter. VAT composite curved panel subjected to in-plane compressive loads. $\theta = [0^\circ \pm (0^\circ/T_1)]_2$.

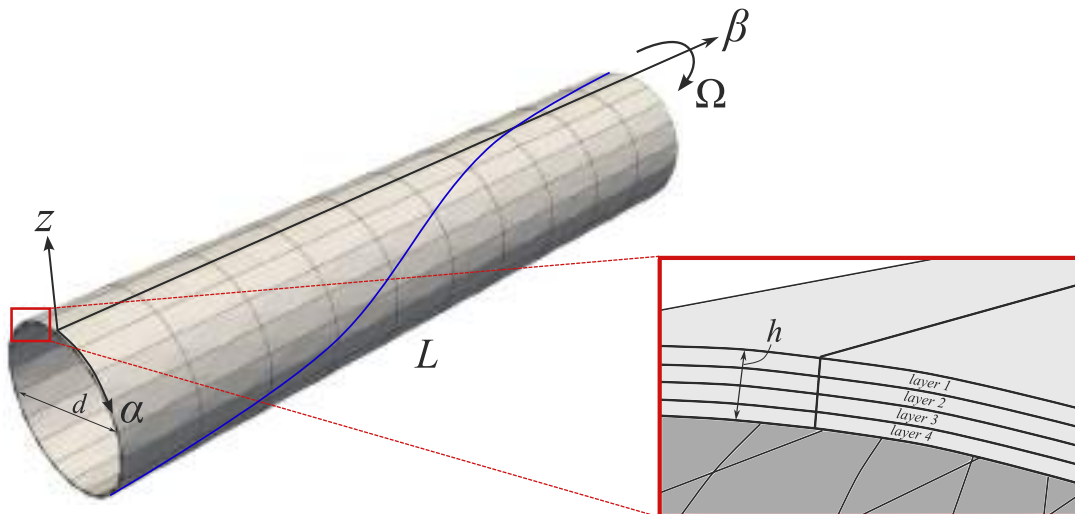


Fig. 7. Geometry and mesh discretization of the VAT composite thin cylinder.

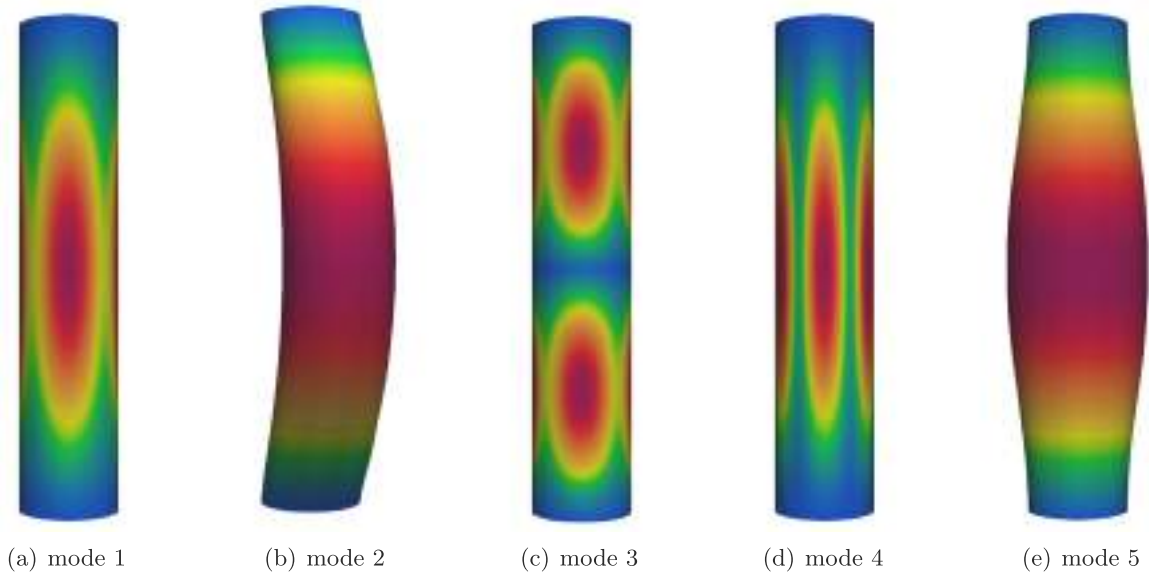


Fig. 8. Mode shapes of the thin cylinder with $[90^\circ/0^\circ]_s$.

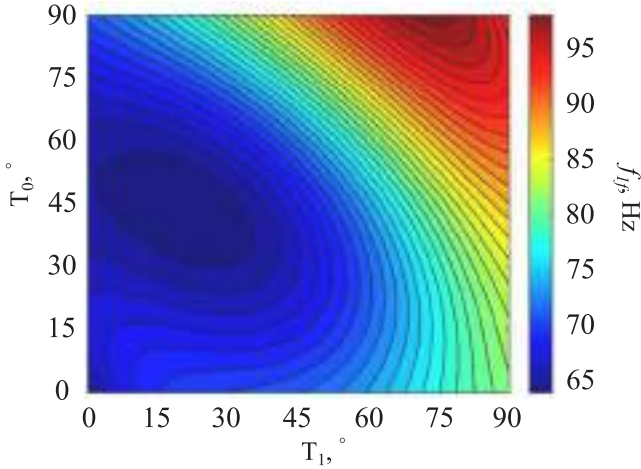


Fig. 9. Effect of T_0 and T_1 parameters on the first natural frequency. Thin cylinder with $\theta = [90^\circ + (T_0/T_1)/0^\circ + (T_0/T_1)]_s$.

where the superscript T denotes transposition. In a total Lagrangian scenario, the displacement–strain relation and the Hooke's law are written as follows:

$$\begin{aligned} \epsilon^k &= \epsilon_l^k + \epsilon_{nl}^k = (b_l + b_{nl})u^k \\ \sigma^k &= \sigma_l^k + \sigma_{nl}^k = C^k(\epsilon_l^k + \epsilon_{nl}^k) \end{aligned} \quad (2)$$

where ϵ^k is the full Green–Lagrange strain tensor, C^k represents the linear elastic matrix for orthotropic materials, b_l and b_{nl} stand for the 6×3 linear and nonlinear differential operators, respectively. For brevity, readers are referred to Refs. [38,39] for details of these matrices.

Since VAT structures are analyzed in this work, the fibers are placed following an arbitrary orientation function of spatial coordinates, i.e., $\theta(\alpha; \beta)$. Therefore, we write:

$$\sigma^k = \tilde{C}^k \epsilon^k \quad (3)$$

where:

$$\tilde{C}^k = T^T C^k T \quad (4)$$

The rotation matrix, denoted by T , represents the orientation of the fibers in VAT structures. In these structures, the fibers have the ability to change along a curved path within each layer. As a result, the laminate exhibits varying stiffness values at different positions. This work considers linear variations in fiber angles across each lamina and employs the expression proposed by Gürdal and Olmedo [40]. It reads:

$$\theta(\alpha') = \Phi + T_0 + \frac{(T_1 - T_0)}{d} |\alpha'| \quad (5)$$

In this scenario, the fiber path undergoes a rotation by an angle θ relative to a specific reference direction. The fiber orientation angle at this reference point is denoted as T_0 and varies along a direction α' , which is oriented at an angle Φ from the original coordinate axis α . At a characteristic distance d from the reference point, the fiber orientation angle becomes T_1 . By considering this rotation angle, the fiber orientation path $\theta(\alpha, \beta)$ can be expressed as $\theta(\alpha')$, where $\alpha' = a \cos \Phi + \beta \sin \Phi$. The parameter d is typically equal to $a/2$ or $b/2$ when $\Phi = 0^\circ$ or $\Phi = 90^\circ$, respectively, where a and b represent the width and length of the 2D structure. Fig. 2 illustrates two fiber path variations in a representative domain.

2.2. Rotordynamics equations in CUF

In this study, the VAT composite shells are modeled within the CUF framework by using classical to high-order shell models. According to CUF, the 3D displacement field is expressed as an arbitrary through-the-thickness expansion of the in-plane variables.

$$u^k(\alpha, \beta, z; t) = F_\tau^k(z) u_\tau^k(\alpha, \beta; t), \quad \tau = 1, \dots, M, \quad (6)$$

in which F_τ^k indicates a set of thickness expansion functions, u_τ^k is the generalized displacement vector, M stands for the order of expansion in the thickness direction, t represents the time and the repeated index indicates summation. The choice of F_τ^k is arbitrary and determines the class of Layerwise (LW) and Equivalent Single Layer (ESL) theories that can be directly developed within CUF. This paper considers both the ESL based on Taylor Expansion (TE) and LW adopting the Lagrange Expansion (LE). The acronyms LDN and TEN, used in the following section, refer to LE and TE of order N , respectively. For example, LD1 stands for the linear (two-node) Lagrange expansion functions, whereas TE1 represents Taylor expansion functions of order one. For a detailed description of these theories, refer to Refs. [41,42].

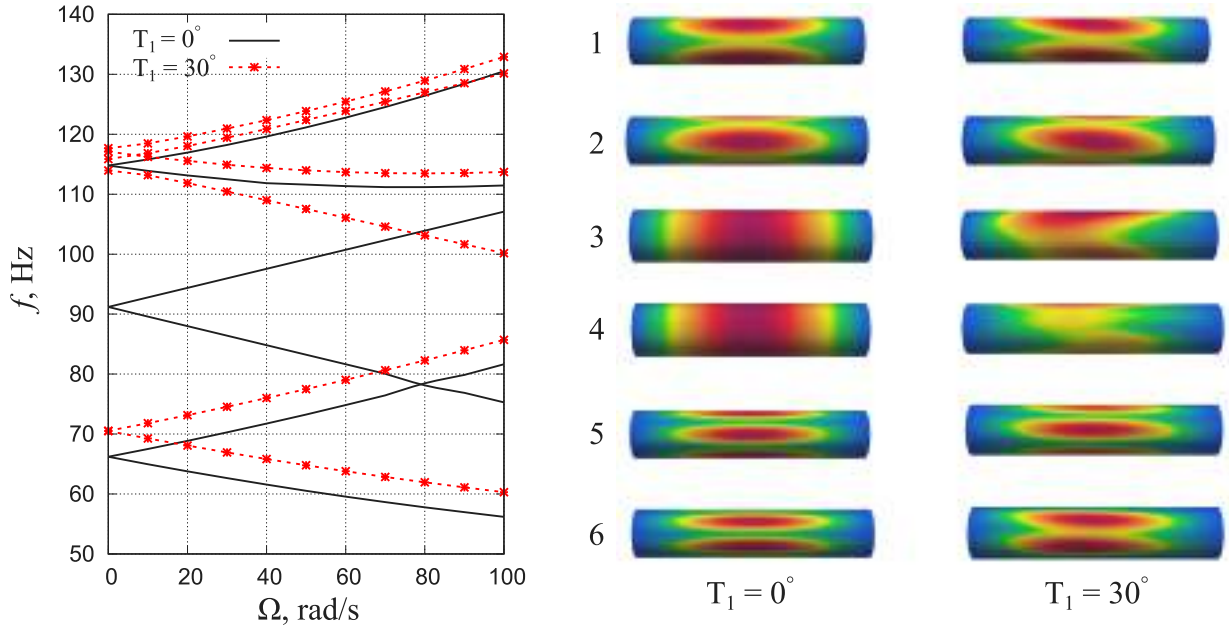


Fig. 10. Frequency variations for various rotational speeds of the thin cylinder with $\theta = [90^\circ + (\theta^\circ/T_1)/0^\circ + (\theta^\circ/T_1)]_1$. Comparison between the classical composite model ($T_1 = 0^\circ$) and the VAT ones ($T_1 = 30^\circ$).

Independently of the selected shell model kinematics, the finite element method (FEM) is employed to approximate the in-plane generalized displacement vector by using shape functions $N_i(\alpha, \beta)$.

$$\mathbf{u}_\tau^k(\alpha, \beta; t) = N_i(\alpha, \beta) \mathbf{q}_{\tau i}^k(t), \quad i = 1, \dots, N_n, \quad (7)$$

in which $\mathbf{q}_{\tau i}^k$ stands for the unknown nodal variables and N_n denotes the number of nodes per element. In this research, the classical 2D nine-node quadratic (Q9) FEs are chosen for the shape functions in the α - β plane.

To derive the nonlinear finite element (FE) governing equations, the Principle of Virtual Work (PVW) is employed.

$$\delta L_{int} + \delta L_{ine} - \delta L_{ext} = 0 \quad (8)$$

where δL_{int} , δL_{ine} and δL_{ext} represent the virtual internal, inertial and external works, respectively. The virtual works are expressed in terms of FNs of the secant stiffness matrix $\mathbf{K}_s^{ij\tau s}$, mass matrix $\mathbf{M}^{ij\tau s}$, Coriolis matrix $\mathbf{G}^{ij\tau s}$, spin softening matrix $\mathbf{K}_\Omega^{ij\tau s}$, centrifugal force vector \mathbf{F}_Ω^{sj} , and nodal force vector \mathbf{F}^{sj} . The superscripts i, j, τ, s are used to assemble the global matrices and vectors. When the structure rotates about the β -axis at a rotational speed Ω , the inertial forces can be expressed as follows:

$$\mathbf{F}_I = -\rho \begin{Bmatrix} \ddot{u}_\alpha \\ \ddot{u}_\beta \\ \ddot{u}_z \end{Bmatrix} - 2\rho\Omega \begin{Bmatrix} \dot{u}_\alpha \\ 0 \\ \dot{u}_z \end{Bmatrix} + \rho\Omega^2 \begin{Bmatrix} u_\alpha \\ 0 \\ u_z \end{Bmatrix} - \rho\Omega^2 \begin{Bmatrix} 0 \\ 0 \\ z_e \end{Bmatrix} \quad (9)$$

$$\begin{aligned} \delta L_{int} &= \int_V \delta \epsilon^T \sigma dV = \delta \mathbf{q}_{sj}^T (\mathbf{K}_0^{ij\tau s} + \mathbf{K}_{lnl}^{ij\tau s} + \mathbf{K}_{nll}^{ij\tau s} + \mathbf{K}_{nl nl}^{ij\tau s}) \mathbf{q}_{\tau i} \\ &= \delta \mathbf{q}_{sj}^T \mathbf{K}_S^{ij\tau s} \mathbf{q}_{\tau i} \\ \delta L_{ine} &= \int_V \delta \dot{\mathbf{u}}^T \mathbf{F}_I dV = \delta \mathbf{q}_{sj}^T (\mathbf{M}^{ij\tau s} \ddot{\mathbf{q}}_{\tau i} + \mathbf{G}^{ij\tau s} \dot{\mathbf{q}}_{\tau i} + \mathbf{K}_\Omega^{ij\tau s} \mathbf{q}_{\tau i} + \mathbf{F}_\Omega^{sj}) \\ \delta L_{ext} &= \delta \mathbf{q}_{sj}^T \mathbf{F}^{sj} \end{aligned} \quad (10)$$

For completeness, complete derivations of the 3-by-3 FNs of Coriolis and spin softening matrices, and the 3-by-1 FN of the centrifugal force vector are reported in Appendix. Further details of these matrices and vectors can be found in Refs. [20,43].

If external loads \mathbf{F} are applied, the nonlinear equation to be solved is:

$$\mathbf{K}_S \mathbf{q}_e = \mathbf{F} + \mathbf{F}_\Omega \quad (11)$$

The solution \mathbf{q}_e is computed with a Newton-Raphson linearization scheme.

Specifically, the FNs of the tangent stiffness matrix (\mathbf{K}_T) and geometric stiffness matrix (\mathbf{K}_σ) are introduced by linearizing the virtual internal work.

$$\delta(\delta L_{int}) = \delta \mathbf{q}_{sj}^T (\mathbf{K}_0^{ij\tau s} + \mathbf{K}_{T1}^{ij\tau s}) \delta \mathbf{q}_{\tau i} + \delta \mathbf{q}_{sj}^T \mathbf{K}_\sigma^{ij\tau s} \delta \mathbf{q}_{\tau i} = \delta \mathbf{q}_{sj}^T \mathbf{K}_T^{ij\tau s} \delta \mathbf{q}_{\tau i} \quad (12)$$

where $\mathbf{K}_T^{ij\tau s}$ indicates the linear component of \mathbf{K}_T , while $\mathbf{K}_{T1}^{ij\tau s} = 2\mathbf{K}_{lnl}^{ij\tau s} + \mathbf{K}_{nll}^{ij\tau s} + 2\mathbf{K}_{nl nl}^{ij\tau s}$ denotes the nonlinear contribution. For a detailed derivation of the tangent stiffness matrix, please refer to Ref. [44].

This work employs a linearized methodology, wherein the stiffness matrix is simplified as:

$$\mathbf{K} \approx \mathbf{K}_0 + \mathbf{K}_\sigma^* \quad (13)$$

The term \mathbf{K}_σ^* is the new geometric stiffness matrix that derives from the nonlinear strain vector multiplied by the linear component of the initial rotation-induced stress vector, which is computed through a linear static analysis, considering the rotational speed $\Omega = 1$ rad/s. To compute the natural frequencies (ω) and their associated mode shapes ($\bar{\mathbf{q}}$) for small-amplitude vibrations, a harmonic solution ($\hat{\mathbf{q}} = \bar{\mathbf{q}} e^{i\omega t}$) is assumed. The quadratic eigenvalue problem is solved following the approach described in Ref. [45].

$$\mathbf{M} \ddot{\hat{\mathbf{q}}} + \Omega \mathbf{G} \dot{\hat{\mathbf{q}}} + (\mathbf{K}_0 + \Omega^2 \mathbf{K}_\sigma^* + \Omega^2 \mathbf{K}_\Omega) \hat{\mathbf{q}} = 0 \quad (14)$$

3. Numerical examples

This section presents an overview of vibration analyses performed on both non-rotating and rotating VAT shell structures. The initial step involves conducting free vibration and buckling analyses on VAT composite curved panels in order to validate the proposed approach. The obtained results are compared with published data and finite element solutions to ensure accuracy. Subsequently, rotordynamics results of various VAT composite thin and thick cylinders are provided. The Mixed Interpolation of Tensorial Components (MITC) technique was adopted to overcome the shear and membrane locking phenomena [46].

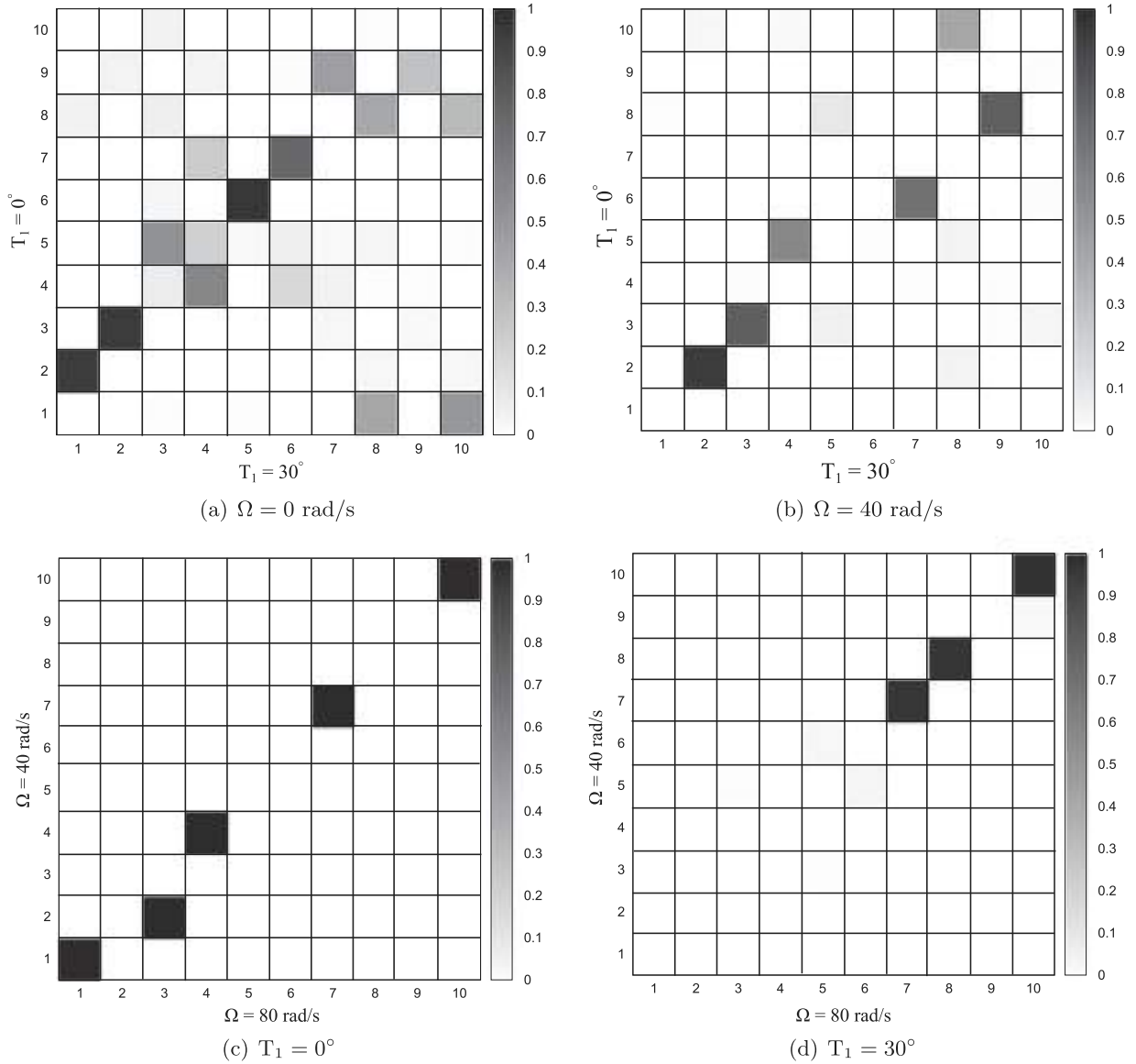


Fig. 11. MAC between the models with $T_1 = 0^\circ$ and $T_1 = 30^\circ$ at different rotational speeds Ω for the thin cylinder with $\theta = [90^\circ + \langle 0^\circ/T_1 \rangle / 0^\circ + \langle 0^\circ/T_1 \rangle]_s$.

3.1. Curved panel

The first example deals with a curved VAT composite panel simply-supported (SS) on all edges. The curved panel's configuration is depicted in Fig. 3. This structure consists of eight composite laminae where the fibers are steered following the stacking sequence: $\theta = [0^\circ \pm \langle 0^\circ/30^\circ \rangle]_{2s}$. This shell model has the following dimensions: $a = b = 0.3$ m and the thickness h is equal to 1.05×10^{-3} m. The material data of the considered structure are: $E_1 = 163$ GPa, $E_2 = 10$ GPa, $G_{12} = 5$ GPa, $\nu_{12} = 0.3$ and $\rho = 1480$ kg/m³.

Firstly, the accuracy of the presented methodology is verified by comparing the free natural frequencies with the results found in the literature or obtained using commercial software. A convergence analysis is conducted to determine the mesh that yields the convergent results. Subsequently, a comparison between ESL and LW models is reported. Table 1 shows the non-rotating natural frequencies for various in-plane mesh approximation. Additionally, Table 2 illustrates the effect of the kinematics theories, from low- to high-order models. The relative errors between the results obtained with and without the MITC correction are provided in brackets. It is evident that the model utilizing a 10×10 Q9

FEs for the in-plane mesh discretization and only one LD1 for each layer achieves good convergence. Table 3 presents a comparison between CUF and FEMAP solutions. In particular, a subroutine was developed to generate FE models consisting of 4-node shell elements (QUAD4), in which the fiber orientations changes element by element. The table demonstrates that the use of the proposed approach allows the adoption of a lighter mesh than that which must be adopted in software such as FEMAP.

Next, buckling analyses of VAT shells subjected to in-plane compressive loads are performed to also validate the geometric stiffness matrix. Considering the previous configuration, the critical buckling load was obtained for various fiber angle orientations. Table 4 shows the critical buckling values obtained through the presented approach and using FEMAP. Additionally, the comparison between the first buckling mode shapes is given in Fig. 4. Moreover, also the effect of the fiber angle orientation T_1 on the critical buckling load was investigated. The related variation is shown in Fig. 5. Fig. 6 displays the first buckling mode shapes as a function of the T_1 parameter. The results suggest that low-order kinematics theories provided similar frequency solutions with those obtained using high-order models. The MITC correction is

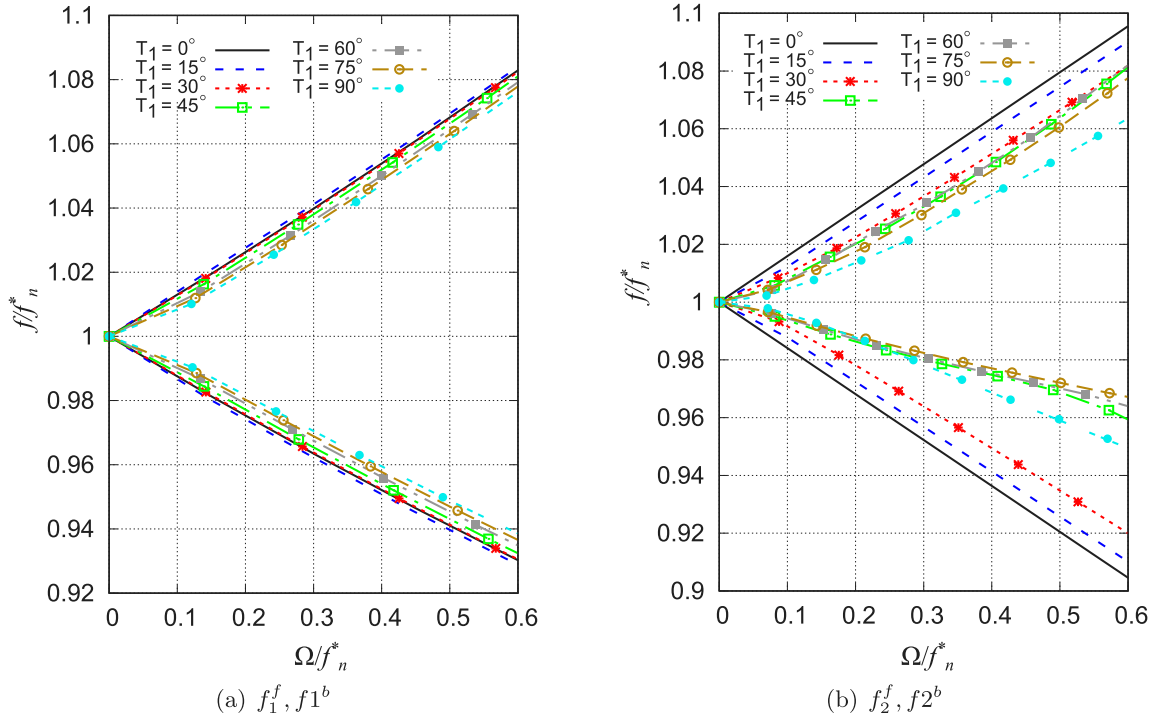


Fig. 12. Effect of T_1 on the Campbell diagram of the first two vibration modes. Thin cylinder with $\theta = [90^\circ + (0^\circ/T_1)]/0^\circ + (0^\circ/T_1)]_s$. f_n^* indicates the value of the considered frequency at $\Omega = 0$ rad/s.

Table 1

Effect of the in-plane mesh approximation on the first ten free natural frequencies [Hz] of the VAT composite curved panel $[0^\circ \pm (0^\circ/30^\circ)]_{2s}$. Lagrange model employing one LD1 for layer. The number of the total degrees of freedom (DOFs) is reported in brackets at the top.

No. mode	Natural frequency			
	5 × 5 Q9 (3267)	10 × 10 Q9 (11907)	20 × 20 Q9 (45387)	30 × 30 Q9 (100467)
1	232.06 ^(-2.38%)	231.12 ^(-1.31%)	230.99 ^(-0.21%)	230.94 ^(-0.06%)
2	236.55 ^(-6.03%)	236.61 ^(-0.08%)	236.52 ^(-0.02%)	236.41 ^(-0.02%)
3	337.97 ^(-4.70%)	336.63 ^(-0.79%)	336.33 ^(-0.14%)	336.15 ^(-0.05%)
4	489.07 ^(-5.33%)	479.18 ^(-2.76%)	478.43 ^(-0.50%)	478.34 ^(-0.14%)
5	493.45 ^(-12.58%)	488.27 ^(-1.12%)	487.59 ^(-0.19%)	487.30 ^(-0.07%)
6	543.02 ^(-6.85%)	534.44 ^(-2.12%)	533.62 ^(-0.36%)	533.40 ^(-0.11%)
7	596.32 ^(-5.55%)	594.87 ^(-0.36%)	594.30 ^(-0.08%)	593.76 ^(-0.05%)
8	630.47 ^(-9.62%)	618.83 ^(-1.98%)	617.68 ^(-0.36%)	617.37 ^(-0.12%)
9	680.54 ^(-6.78%)	663.87 ^(-1.41%)	662.19 ^(-0.30%)	661.73 ^(-0.12%)
10	770.22 ^(-7.88%)	748.32 ^(-2.22%)	746.19 ^(-0.44%)	745.78 ^(-0.16%)

Table 2

Effect of kinematics theories on the natural frequencies [Hz]. VAT composite curved panel $[0^\circ \pm (0^\circ/30^\circ)]_{2s}$. 10 × 10 Q9 model.

No. mode	Natural frequency							
	LD1 (11907)	LD2 (22491)	LD3 (33075)	CLT (1323)	FSDT (2205)	TE1 (2646)	TE2 (3969)	TE3 (5292)
1	231.12	231.08	231.08	233.51	232.32	232.73	231.16	231.11
2	236.61	236.48	236.47	243.90	243.88	237.04	236.76	236.75
3	336.63	336.54	336.54	342.15	341.86	339.23	336.74	336.65
4	479.18	479.08	479.08	483.23	482.53	482.44	479.31	479.14
5	488.27	488.07	488.07	496.27	495.90	492.78	488.50	488.37
6	534.44	534.26	534.26	540.89	540.08	538.66	534.67	534.45
7	594.87	594.35	594.32	605.04	604.89	596.63	595.52	595.44
8	618.83	618.54	618.53	628.59	627.71	625.85	619.14	618.84
9	663.87	663.65	663.65	674.33	673.66	671.15	664.15	663.97
10	748.32	747.96	747.95	761.89	760.80	758.52	748.63	748.28

crucial when utilizing a coarse mesh, as it can significantly affect the results. However, when using a finer mesh, the MITC correction does not have a noticeable impact on the outcome. The CUF solutions are in good agreement with the FEMAP ones. Finally, in the considered case, increasing the parameter T_1 led to an increase in the critical buckling load value.

3.2. Thin cylinder

The second example concerns a clamped-clamped thin variable-angle-tow composite cylinder, analyzed in both rotating and non-rotating conditions. The material properties are as follows: the elastic Young moduli $E_1 = 224$ GPa, $E_2 = E_3 = 12.7$ GPa, shear moduli

Table 3
Natural frequencies [Hz] of the VAT composite curved panel $[0^\circ \pm (0^\circ/30^\circ)]_{2s}$.

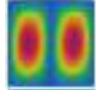
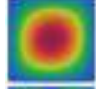

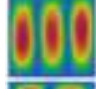

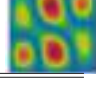
No. mode	Natural frequency			Mode shape
	Present (10×10 Q9+LD1)	FEMAP (10×10)	FEMAP (100×100)	
1	231.12	228.15	231.70	
2	236.61	237.44	237.76	
3	336.63	329.51	338.39	
4	479.18	471.80	478.98	
5	488.27	472.94	490.82	
6	534.44	514.78	533.73	

Table 4
First linearized buckling load value of the VAT composite curved panel $[0^\circ \pm (0^\circ/30^\circ)]_{2s}$.

Model	P_{cr} [N/m]
Present (10 × 10 Q9+LD1)	12172.79
FEMAP (100 × 100)	12032.65

$G_{12} = G_{23} = G_{13} = 4.42$ GPa, Poisson ratio $\nu_{12} = 0.256$, and density $\rho = 2527$ kg/m³. The dimensions are: length $L = 5$ m, thickness $t = 0.02$ and the diameter is equal to 1 m. This particular structure, illustrated in Fig. 7, has been previously examined in unstiffened and stiffened isotropic and classical composite configurations [20,21,43].

Table 5 shows the first five non-rotating natural frequencies of the thin cylinder, computed using various meshes, including the comparison with the FEMAP solution. Specifically, various discretization from 32 Q9 to 288 Q9 FEs are considered for the surface approximation, while one LD1 is employed along the thickness. The 20×10 Q9 mesh provided a reliable approximation for the in-plane description. Table 6 provided the effect of the kinematic theory on the non-rotating natural frequencies. For completeness, the mode shapes of the first five frequencies are depicted in Fig. 8. The results suggest that low-order models (LD1) are sufficient to accurately predict the frequencies, while some discrepancies are noted when the classical theories (Classical lamination theory (CLT), First shear deformation theory (FSDT)) or TE1 are employed. Furthermore, the importance of considering the MITC locking correction in the analysis of thin cylinders is evident in Table 7. Notably, substantial disparities arise when employing coarse meshes, with differences reaching approximately a maximum of 48.21%. Although the percentage gap diminishes (a maximum of 13.80%) with the adoption of a finer mesh, disparities persist between results with and without the MITC correction. The incorporation of MITC correction enables the utilization of significantly lighter meshes, providing a significant computational advantage. Table 8 provides a comparison between the CUF frequency solutions and those achieved using the commercial software FEMAP for the thin cylinder with the lamination $\theta = [90^\circ + (0^\circ/15^\circ)/0^\circ + (0^\circ/15^\circ)]_s$. Some discrepancies are observed, which can be attributed to variations in the application of VAT rolling. In particular, commercial software tools typically assume a constant lamination angle throughout the entire element domain, while the proposed methodology allows for the fiber angle to vary

at each Gaussian point within the shell element. The effect of the T_0 and T_1 parameters variation on the first natural frequency for the thin cylinder with lamination $\theta = [90^\circ + (T_0/T_1)/0^\circ + (T_0/T_1)]_s$ is shown in Fig. 9. It is noted the maximum value of the first natural frequency is obtained adopting $T_0 = 90^\circ$ and $T_1 = 75^\circ$. The specific numerical values for the forward and backward first and second vibration modes can be found in Tables 9 and 10. In contrast to a classical composite material where the frequencies for forward and backward behavior are identical, a variable lamination introduces a slight difference between these values. This discrepancy becomes evident when T_0 and T_1 are not equal. Fig. 10 depicts the frequency variations with respect to the rotational speed for the thin cylinder, comparing the solutions obtained using $T_1 = 0^\circ$ or $T_1 = 30^\circ$. The same figure shows the vibration mode shapes for the two models analyzed. It is evident that the use of a VAT models led to increase the frequencies. For completeness, a comparison of the first ten vibration mode shapes of the thin cylinder is conducted for two cases: $T_1 = 0^\circ$ or $T_1 = 30^\circ$. The comparison utilizes a Modal Assurance Criterion (MAC) graphical representation, as illustrated in Fig. 11. MAC is a scalar that measures the similarity between two sets of mode shapes [47,48]. Specifically, Fig. 11a and b illustrate the comparison of frequencies between the two models at $\Omega = 0$ rad/s and $\Omega = 40$ rad/s, respectively. Instead, Fig. 11c and d provide the frequency changes within the same model at two different rotational speed values. The effect of the T_1 parameter on the Campbell diagram for the first two vibration modes is presented in Fig. 12, showing that as the T_1 value increases the structure shows a stiffer behavior, i.e., the frequencies increase. Table 11 provides the specific numerical values for the forward and backward second vibration mode for different T_0 and T_1 combinations at $\Omega = 50$ rad/s.

3.3. Thick cylinder

The last case deals with a VAT composite thick cylinder. For this case, both stress and vibration analyses with different boundary conditions are presented. The dimensions of this structure are: thickness equal to 0.0381 m, length is 0.254 m, and mean radius equal to 0.09525 m. The material data are the following: $E_1 = 224$ GPa, $E_2 = E_3 = 12.7$ GPa, $G_{12} = G_{23} = G_{13} = 4.42$ GPa, $\nu_{12} = 0.256$, and $\rho = 2527$ kg/m³. After convergence studies, 12×6 Q9 FEs were adopted for the in-plane mesh discretization.

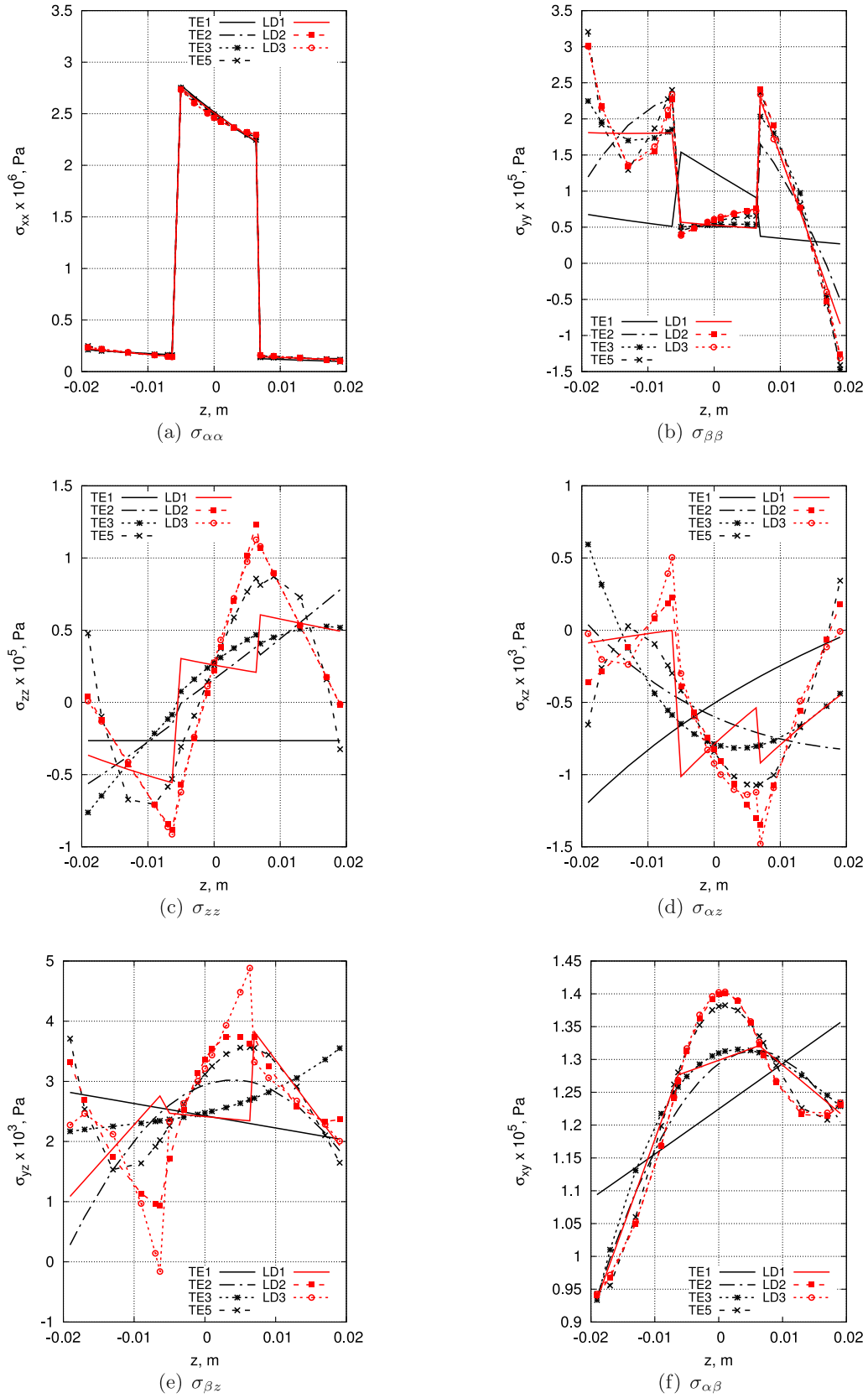


Fig. 13. Through-the-thickness stress distributions for the clamped-clamped VAT composite thick cylinder with $\theta = [90^\circ + \langle 0^\circ/30^\circ \rangle / 0^\circ + \langle 0^\circ/30^\circ \rangle / 90^\circ + \langle 0^\circ/30^\circ \rangle]$, considering various kinematics theories and $\Omega = 200$ rad/s.

In order to show the effectiveness of this methodology in calculating the stresses and emphasize the importance of adopting high-fidelity

models, Fig. 13 depicts the 3D stress distributions along the thickness at the structure's center, comparing low- and high-order kinematics

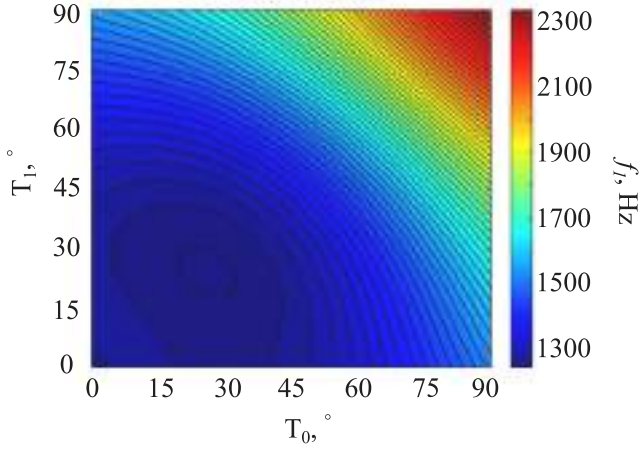


Fig. 14. Effect of T_0 and T_1 parameters on the first natural frequency. Free-free VAT composite thick cylinder with $\theta = [90^\circ + \langle T_0/T_1 \rangle / 0^\circ + \langle T_0/T_1 \rangle / 90^\circ + \langle T_0/T_1 \rangle]$.

Table 5

Natural frequencies [Hz] at standstill of the thin cylinder with $[90^\circ/0^\circ]_s$ for different in-plane mesh approximations using one LD1 for layer, along with the DOFs.

Model	No. mode				
	1	2	3	4	5
8×4 Q9+LD1 (2160)	66.33	91.49	116.69	120.92	132.29
12×6 Q9+LD1 (4680)	66.23	91.24	115.95	116.72	132.26
14×8 Q9+LD1 (7140)	66.21	91.20	115.34	116.64	132.26
20×10 Q9+LD1 (12600)	66.21	91.19	114.77	116.65	132.25
24×12 Q9+LD1 (18000)	66.21	91.18	114.70	116.65	132.25
FEMAP (125 \times 78)	66.18	91.10	114.55	116.58	132.17

Table 6

Effect of the kinematics theories on the natural frequencies [Hz] at standstill of the thin cylinder with $[90^\circ/0^\circ]_s$. Model with 20×10 Q9.

Model	No. mode				
	1	2	3	4	5
LD1 (12600)	66.21	91.19	114.77	116.65	132.25
LD2 (22680)	66.17	91.18	114.57	116.62	132.25
LD3 (32760)	66.17	91.18	114.57	116.62	132.25
CLT (2520)	66.76	91.44	117.02	117.40	132.25
FSDT (4200)	65.58	90.65	114.41	114.79	132.25
TE1 (5040)	65.57	90.65	114.40	114.77	132.25
TE2 (7560)	66.23	91.20	115.04	116.69	132.25
TE3 (10080)	66.19	91.18	114.70	116.63	132.25

theories. The results suggest that low-order ESL models are sufficient to predict the in-plane circumferential normal stress ($\sigma_{\alpha\alpha}$) distribution. In contrast, when shear stresses are calculated through the Hooke's Law, higher-order LW theories are necessary. In fact, ESL models are not able to describe the distribution, even if high-order theories (i.e., TE5) are considered. The transverse shear stress plot points out that the traction-free conditions at the top and bottom positions are satisfied only by considering the cubic Lagrange polynomials (LD3). The TE5 solutions show good agreement with the LD2 and LD3 models for both normal, $\sigma_{\beta\beta}$, and in-plane shear, $\sigma_{\alpha\beta}$, stresses. Table 12 provides the first ten non-rotating natural frequencies of the thick cylinder with lamination $\theta = [90^\circ + \langle 0^\circ/30^\circ \rangle / 0^\circ + \langle 0^\circ/30^\circ \rangle / 90^\circ + \langle 0^\circ/30^\circ \rangle]$. The table includes a comparison between different kinematics theories and also provides the associated mode shapes. The results highlight the significant inaccuracies that emerge when applying the classical theory to a thick cylindrical structure. The LD1 model will be adopted for the following analyses. The influence of T_0 and T_1 parameters on the first natural frequency of the thick cylinder is illustrated in Fig. 14. It is evident that the highest frequency value is achieved when both T_0 and

Table 7

Effect of locking correction on the natural frequencies [Hz] for two different mesh approximations. Thin cylinder with $[0^\circ/90^\circ]_s$.

8×4 Q9 + LD1				
No. mode	f (MITC)	Mode shape	f (NO MITC)	Mode shape
1	66.33		99.40	
2	91.49		132.29	
3	116.69		176.65	
4	120.92		194.08	
5	132.29		208.30	
20×10 Q9 + LD1				
No. mode	f (MITC)	Mode shape	f (NO MITC)	Mode shape
1	66.21		72.71	
2	91.19		92.01	
3	114.78		121.92	
4	116.66		132.25	
5	132.25		135.33	

T_1 are set to 90° . Fig. 15 presents the Campbell diagrams of the first two vibration modes for three different models: (A): classical composite; (B) $T_0 = 0^\circ$ and $T_1 = 30^\circ$; (C) $T_0 = 75^\circ$ and $T_1 = 30^\circ$. The results show that Model C is more rigid than the others. Furthermore, Tables 13 and 14 provide the specific numerical values of the first and second vibration modes for various combinations of T_0 and T_1 when $\Omega = 0$ rad/s. For completeness, the MAC graphical representation between the modes of the thick cylinder with $T_0 = 0^\circ$ and $T_1 = 30^\circ$ at two different rotational speeds ($\Omega = 400$ rad/s versus $\Omega = 800$ rad/s) is presented in Fig. 16. The figure demonstrates the mode changes that occur as the rotational speeds progressively increase.

4. Conclusions

Rotordynamics analyses of various variable-angle-tow (VAT) composite curved panels and thin and thick cylinders were conducted using low- and high-fidelity models. Two-dimensional (2D) shell finite elements formulated in the Carrera Unified Formulation (CUF) framework were employed to model these structures. The equations of motion were derived in a co-rotating frame of reference, including all rotational speed contributions, such as Coriolis and spin softening effects. For computational efficiency, a linearized approach was employed to

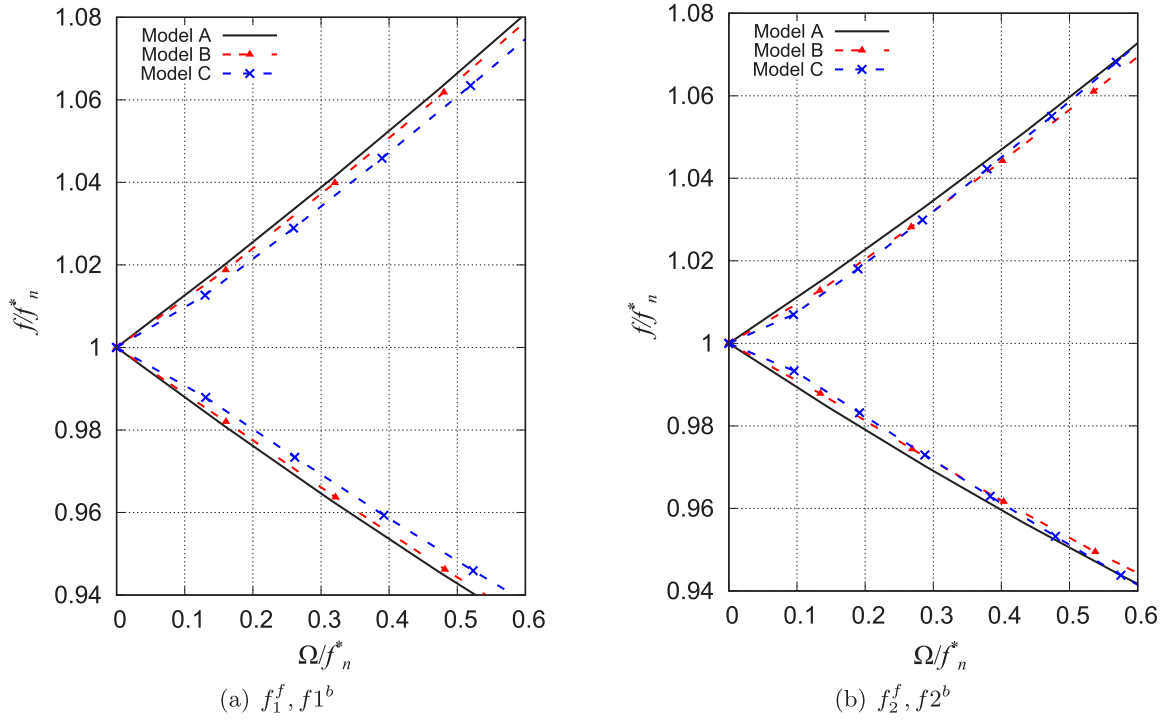


Fig. 15. Campbell diagrams of the free-free thick cylinder with: Model A = $[90^\circ/0^\circ/90^\circ]$; Model B = $[90^\circ + \langle 0^\circ/30^\circ \rangle / 0^\circ + \langle 0^\circ/30^\circ \rangle / 90^\circ + \langle 0^\circ/30^\circ \rangle]$; Model C = $[90^\circ + \langle 75^\circ/30^\circ \rangle / 0^\circ + \langle 75^\circ/30^\circ \rangle / 90^\circ + \langle 75^\circ/30^\circ \rangle]$. f_n^* indicates the value of the associated frequency at $\Omega = 0$ rad/s.

Table 8

Comparison between CUF and FEMAP frequency solutions [Hz]. Thin cylinder with $\theta = [90^\circ + \langle 0^\circ/15^\circ \rangle / 0^\circ + \langle 0^\circ/15^\circ \rangle]$.

No. mode	20 × 10 Q9 + LD1			FEMAP		
	f (MITC)	Mode shape	f (NO MITC)	Mode shape	f	Mode shape
1	68.61		74.80		66.42	
2	68.78		74.96		66.43	
3	99.19		100.01		91.41	
4	99.96		100.82		91.95	
5	114.71		131.03		113.73	
6	114.71		131.11		113.75	

investigate several cylindrical structures. It was observed that, in many cases, a low-order shell model proved sufficient to accurately capture the dynamic response of rotating structures. Practical examples were utilized to showcase the capabilities of the presented approach and

provide benchmark solutions. The numerical results demonstrated the accuracy and reliability of the proposed methodology and highlighted the potential of the presented numerical tool.

Table 9

Variation of the first vibration mode [Hz] as a function of the T_0 and T_1 parameters at $\Omega = 0$ rad/s. Thin cylinder with $\theta = [90^\circ + \langle T_0/T_1 \rangle / 0^\circ + \langle T_0/T_1 \rangle]_s$.

$T_0 - T_1$	0°		15°		30°		45°		60°		75°		90°	
	f_1^f	f_1^b	f_1^f	f_1^b	f_1^f	f_1^b	f_1^f	f_1^b	f_1^f	f_1^b	f_1^f	f_1^b	f_1^f	f_1^b
0°	66.21	66.21	68.61	68.78	70.48	70.53	71.85	72.11	74.40	74.97	78.19	79.00	81.66	82.80
15°	67.00	67.16	68.32	68.32	68.02	68.01	69.22	69.56	72.60	73.21	77.60	78.41	82.37	83.34
30°	65.90	65.92	64.38	64.74	65.14	65.14	67.35	67.44	71.95	72.16	78.25	78.46	84.41	84.53
45°	64.75	65.17	64.98	64.74	65.18	65.28	68.61	68.61	74.25	74.26	81.43	81.50	88.24	88.50
60°	65.42	66.16	65.99	66.60	68.19	68.38	72.85	72.86	79.36	79.36	87.09	87.13	93.49	93.70
75°	67.89	68.80	69.98	70.70	73.82	73.98	79.75	79.83	87.11	87.15	94.53	94.53	93.93	94.40
90°	71.62	72.40	75.32	76.08	81.10	81.10	88.26	88.57	95.57	95.92	98.93	99.19	90.64	90.64

Table 10

Variation of the second vibration mode [Hz] as a function of the T_0 and T_1 parameters at $\Omega = 0$ rad/s. Thin cylinder with $\theta = [90^\circ + \langle T_0/T_1 \rangle / 0^\circ + \langle T_0/T_1 \rangle]_s$.

$T_0 - T_1$	0°		15°		30°		45°		60°		75°		90°	
	f_2^f	f_2^b	f_2^f	f_2^b	f_2^f	f_2^b	f_2^f	f_2^b	f_2^f	f_2^b	f_2^f	f_2^b	f_2^f	f_2^b
0°	66.21	66.21	99.19	99.96	113.95	115.87	122.41	123.12	131.18	133.28	139.64	140.48	140.38	143.92
15°	95.70	96.35	111.64	111.64	115.11	115.23	122.46	122.85	131.96	132.56	140.92	143.54	138.77	145.47
30°	103.32	105.52	109.52	109.64	115.37	115.37	125.40	125.44	132.40	135.23	129.64	137.56	118.54	131.39
45°	108.16	108.24	111.21	111.64	120.02	120.07	130.77	130.77	129.69	130.77	123.88	127.98	111.45	116.85
60°	111.01	111.32	116.37	117.01	127.33	128.39	131.30	132.34	129.13	129.13	118.20	118.99	103.22	103.70
75°	116.29	117.01	124.95	126.32	130.07	134.93	135.19	138.27	131.23	131.45	111.86	111.86	99.06	99.23
90°	123.32	125.20	132.67	139.19	132.54	140.03	135.45	140.86	123.27	124.09	100.43	100.69	101.10	101.10

Table 11

Variation of the second vibration mode [Hz] as a function of the T_0 and T_1 parameters at $\Omega = 50$ rad/s. Thin cylinder with $\theta = [90^\circ + \langle T_0/T_1 \rangle / 0^\circ + \langle T_0/T_1 \rangle]_s$.

$T_0 - T_1$	0°		15°		30°		45°		60°		75°		90°	
	f_2^f	f_2^b	f_2^f	f_2^b	f_2^f	f_2^b	f_2^f	f_2^b	f_2^f	f_2^b	f_2^f	f_2^b	f_2^f	f_2^b
0°	83.23	99.14	91.76	107.41	107.54	122.36	119.27	129.09	127.05	137.12	130.68	136.74	120.75	136.61
15°	88.20	103.87	108.45	118.01	111.95	121.52	119.34	128.99	128.24	138.62	129.94	139.09	120.42	137.29
30°	96.85	112.01	106.42	116.03	112.20	122.21	112.09	131.77	126.89	142.45	125.66	139.11	115.39	133.74
45°	102.02	114.41	108.24	117.94	116.78	126.48	123.36	138.24	122.82	137.75	118.20	133.26	106.28	122.00
60°	105.26	117.16	113.07	123.29	122.01	134.55	124.48	139.30	121.55	136.74	110.89	126.31	95.88	111.11
75°	108.30	122.49	117.22	130.99	125.49	136.90	129.39	144.62	124.16	139.53	104.01	119.72	93.19	106.01
90°	109.74	121.63	119.50	132.60	128.70	142.25	130.38	145.21	116.02	131.27	94.33	107.92	95.19	107.91

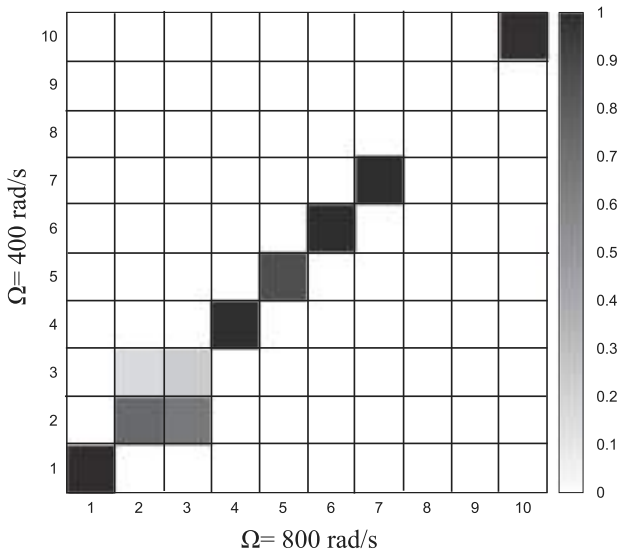


Fig. 16. MAC between two different rotational speeds Ω for the free-free VAT composite thick cylinder with $T_0 = 0^\circ$ and $T_1 = 30^\circ$.

CRediT authorship contribution statement

R. Azzara: Writing – original draft, Visualization, Investigation. **M. Filippi:** Writing – review & editing, Supervision, Software. **E. Carrera:** Methodology, Funding acquisition, Conceptualization.

Declaration of competing interest

The authors declare that they have no known competing financial interests or personal relationships that could have appeared to influence the work reported in this paper.

Data availability

No data was used for the research described in the article.

Appendix. Derivation of FNs

Consider shells with constant thickness and constant radii of curvature R_α and R_β , and rotating around the y -axis. So, we have:

$$H_\alpha = \left(1 + \frac{\zeta}{R_\alpha}\right), \quad H_\beta = \left(1 + \frac{\zeta}{R_\beta}\right) \quad (15)$$

where ζ stands for the distance of the point from the reference surface. Particularly, cases with $H_\beta = 1$, i.e., only curvature R_α , are considered in this work. For brevity, $\langle \cdot \rangle = \int_V (\cdot) dV$.

A.1. Coriolis matrix

$$\begin{aligned} G^{ijrs}[1, 3] &= 2\rho \langle F_\tau F_s N_i N_j H_\alpha \rangle \Omega \\ G^{ijrs}[3, 1] &= -2\rho \langle F_\tau F_s N_i N_j H_\alpha \rangle \Omega \end{aligned} \quad (16)$$

Table 12

Natural frequencies [Hz] of the free-free VAT composite thick cylinder with $\theta = [90^\circ + \langle 0^\circ/30^\circ \rangle / 0^\circ + \langle 0^\circ/30^\circ \rangle / 90^\circ + \langle 0^\circ/30^\circ \rangle]$. 12×6 Q9 model.

No. mode	Natural frequency					Mode shape
	CLT (936)	TE3 (3744)	LD1 (3744)	LD2 (6552)	LD3 (9750)	
1	1490.85	1247.16	1245.27	1236.10	1228.64	
2	1497.59	1250.86	1248.88	1239.74	1232.09	
3	1836.23	1483.54	1487.51	1473.66	1467.15	
4	1845.15	1489.50	1494.03	1479.83	1473.48	
5	2825.22	2786.37	2787.41	2783.22	2782.91	
6	3052.03	2949.24	2951.91	2941.89	2941.02	
7	3146.14	3041.71	3043.73	3033.79	3029.85	
8	4150.45	3111.87	3110.18	3078.62	3057.59	
9	4155.33	3117.19	3115.83	3085.57	3067.07	
10	4534.48	3370.68	3378.98	3340.50	3322.77	

Table 13

Variation of the first vibration mode [Hz] as a function of the T_0 and T_1 parameters at $\Omega = 0$ rad/s. Free-free thick cylinder with $\theta = [90^\circ + \langle T_0/T_1 \rangle / 0^\circ + \langle T_0/T_1 \rangle / 90^\circ + \langle T_0/T_1 \rangle]$.

$T_0 - T_1$	0°		30°		75°	
	f_1^f	f_1^b	f_1^f	f_1^b	f_1^f	f_1^b
0°	1270.34	1270.34	1245.27	1248.88	1410.49	1429.78
30°	1252.69	1257.02	1251.23	1251.23	1523.33	1532.50
75°	1432.86	1454.02	1528.92	1539.88	2025.25	2025.25

Table 14

Variation of the second vibration mode [Hz] as a function of the T_0 and T_1 parameters at $\Omega = 0$ rad/s. Free-free thick cylinder with $\theta = [90^\circ + \langle T_0/T_1 \rangle / 0^\circ + \langle T_0/T_1 \rangle / 90^\circ + \langle T_0/T_1 \rangle]$.

$T_0 - T_1$	0°		30°		75°	
	f_2^f	f_2^b	f_2^f	f_2^b	f_2^f	f_2^b
0°	1384.10	1384.10	1487.51	1494.03	1423.81	1746.34
30°	1526.43	1533.87	1723.87	1723.87	2010.19	2031.09
75°	1829.08	1855.17	2085.65	2110.57	2378.69	2378.69

A.2. Spin softening matrix

$$\mathbf{K}_{\Omega}^{ijrs}[1, 1] = -\rho \langle F_r F_s N_i N_j H_\alpha H_\beta \rangle \Omega^2 \quad (17)$$

$$\mathbf{K}_{\Omega}^{ijrs}[3, 3] = -\rho \langle F_r F_s N_i N_j H_\alpha H_\beta \rangle \Omega^2$$

A.3. Centrifugal force vector

$$\mathbf{F}_{\Omega}^{Sj}[3] = \rho z_e \langle F_s N_j H_\alpha R_\alpha \rangle \Omega^2 \quad (18)$$

References

- [1] A.E.H. Love, *Mathematical Theory of Elasticity*, Cambridge University Press, 2013.
- [2] L.H. Donnell, A new theory for the buckling of thin cylinders under axial compression and bending, *Trans. Am. Soc. Mech. Eng.* 56 (8) (1934) 795–806.
- [3] J.L. Sanders Jr., An improved first-order approximation theory for thin shells, *NASA Tech. Rep.* 1 (1959).
- [4] A.W. Leissa, *Vibration of Shells*, (NASA SP-288), US Government Printing Office, Washington, DC, USA, 1973.
- [5] R.D. Mindlin, Influence of rotatory inertia and shear flexural motions of isotropic elastic plates, *J. Appl. Mech.* 18 (1951) 1031–1036.
- [6] E. Reissner, The effect of transverse shear deformation on the bending of elastic plates, *J. Appl. Mech.* 12 (1945) 69–76.
- [7] J.N. Reddy, C.F. Liu, A higher-order shear deformation theory of laminated elastic shells, *Internat. J. Engrg. Sci.* 23 (3) (1985) 319–330.
- [8] E. Carrera, Theories and finite elements for multilayered plates and shells: a unified compact formulation with numerical assessment and benchmarking, *Arch. Comput. Methods Eng.* 10 (3) (2003) 215–296.
- [9] G.H. Bryan, On the beats in the vibrations of a revolving cylinder or bell, in: *Proceedings of the Cambridge Philosophical Society*, Vol. 7, 1890, pp. 101–111.
- [10] R.A. DiTaranto, M. Lessen, Coriolis acceleration effect on the vibration of a rotating thin-walled circular cylinder, *J. Appl. Mech.* 31 (1964) 700–701.
- [11] J. Padovan, Natural frequencies of rotating prestressed cylinders, *J. Sound Vib.* 31 (4) (1973) 469–482.
- [12] O. Rand, Y. Stavsky, Free vibrations of spinning composite cylindrical shells, *Int. J. Solids Struct.* 28 (7) (1991) 831–843.
- [13] Y. Chen, H.B. Zhao, Z.P. Shen, I. Grieger, B.H. Kröplin, Vibrations of high speed rotating shells with calculations for cylindrical shells, *J. Sound Vib.* 160 (1) (1993) 137–160.
- [14] P.W. Loveday, C.A. Rogers, Free vibration of elastically supported thin cylinders including gyroscopic effects, *J. Sound Vib.* 217 (3) (1998) 547–562.
- [15] K.Y. Lam, C.T. Loy, On vibrations of thin rotating laminated composite cylindrical shells, *Compos. Eng.* 4 (11) (1994) 1153–1167.
- [16] Y.S. Lee, Y.W. Kim, Vibration analysis of rotating composite cylindrical shells with orthogonal stiffeners, *Comput. Struct.* 69 (2) (1998) 271–281.
- [17] X. Zhao, K.M. Liew, T.Y. Ng, Vibrations of rotating cross-ply laminated circular cylindrical shells with stringer and ring stiffeners, *Int. J. Solids Struct.* 39 (2) (2002) 529–545.

- [18] K.R. Sivasdas, Vibration analysis of pre-stressed rotating thick circular conical shell, *J. Sound Vib.* 186 (1) (1995) 99–109.
- [19] D. Guo, F.L. Chu, Z.C. Zheng, The influence of rotation on vibration of a thick cylindrical shell, *J. Sound Vib.* 242 (3) (2001) 487–505.
- [20] M. Filippi, R. Azzara, E. Carrera, Rotordynamic analyses with variable-kinematic beam and shell finite elements, *Mech. Adv. Mater. Struct.* (2023) 1–13.
- [21] R. Azzara, M. Filippi, E. Carrera, Rotordynamic analyses of stiffened cylindrical structures using high-fidelity shell models, *Mech. Adv. Mater. Struct.* (2024) 1–10.
- [22] B.C. Kim, K. Potter, P.M. Weaver, Continuous tow shearing for manufacturing variable angle tow composites, *Composites A* 43 (8) (2012) 1347–1356.
- [23] H.J.A.L. Dirk, C. Ward, K.D. Potter, The engineering aspects of automated prepreg layup: History, present and future, *Composites B* 43 (3) (2012) 997–1009.
- [24] M.W. Hyer, H.H. Lee, The use of curvilinear fiber format to improve buckling resistance of composite plates with central circular holes, *Compos. Struct.* 18 (3) (1991) 239–261.
- [25] M.W. Hyer, R.F. Charette, Use of curvilinear fiber format in composite structure design, *AIAA J.* 29 (6) (1991) 1011–1015.
- [26] K. Schueler, R. Hale, Object-oriented implementation of an integrated design and analysis tool for fiber placed structures, in: 43rd AIAA/ASME/ASCE/AHS/ASC Structures, Structural Dynamics, and Materials Conference, 2002, p. 1223.
- [27] B.F. Tatting, Z. Gurdal, Automated Finite Element Analysis of Elastically-Tailored Plates, NASA/CR-2003-212679, 2003.
- [28] D. Peeters, M. Abdalla, Design guidelines in nonconventional composite laminate optimization, *J. Aircr.* 54 (4) (2017) 1454–1464.
- [29] J.M.J.F. Van Campen, C. Kassapoglou, Z. Gürdal, Generating realistic laminate fiber angle distributions for optimal variable stiffness laminates, *Composites B* 43 (2) (2012) 354–360.
- [30] S.C. White, G. Raju, P.M. Weaver, Initial post-buckling of variable-stiffness curved panels, *J. Mech. Phys. Solids* 71 (2014) 132–155.
- [31] A.R. Sánchez-Majano, R. Azzara, A. Pagani, E. Carrera, Accurate stress analysis of variable angle tow shells by high-order equivalent-single-layer and layer-wise finite element models, *Materials* 14 (21) (2021) 6486.
- [32] B.F. Tatting, Analysis and Design of Variable Stiffness Composite Cylinders (Ph.D. thesis), Virginia Tech, 1998.
- [33] K.C. Wu, Design and analysis of tow-steered composite shells using fiber placement, in: American Society for Composites 23rd Annual Technical Conference, 2008.
- [34] S.C. White, P.M. Weaver, Towards imperfection insensitive buckling response of shell structures-shells with plate-like post-buckled responses, *Aeronaut. J.* 120 (1224) (2016) 233–253.
- [35] A.W. Blom, B.F. Tatting, J.M.A.M. Hol, Z. Gürdal, Fiber path definitions for elastically tailored conical shells, *Composites B* 40 (1) (2009) 77–84.
- [36] F. Tornabene, N. Fantuzzi, M. Baccocchi, E. Viola, Higher-order theories for the free vibrations of doubly-curved laminated panels with curvilinear reinforcing fibers by means of a local version of the GDQ method, *Composites B* 81 (2015) 196–230.
- [37] E. Carrera, M. Cinefra, M. Petrolo, E. Zappino, Finite Element Analysis of Structures Through Unified Formulation, John Wiley & Sons, 2014.
- [38] K.J. Bathe, Finite Element Procedure, Prentice Hall, Upper Saddle River, New Jersey, USA, 1996.
- [39] E. Carrera, A. Pagani, R. Augello, B. Wu, Popular benchmarks of nonlinear shell analysis solved by 1D and 2D CUF-based finite elements, *Mech. Adv. Mater. Struct.* (2020) 1–12.
- [40] Z. Gurdal, R. Olmedo, In-plane response of laminates with spatially varying fiber orientations-variable stiffness concept, *AIAA J.* 31 (4) (1993) 751–758.
- [41] E. Carrera, Multilayered shell theories accounting for layerwise mixed description, part 1: governing equations, *AIAA J.* 37 (9) (1999) 1107–1116.
- [42] A. Pagani, R. Azzara, R. Augello, E. Carrera, Stress states in highly flexible thin-walled composite structures by unified shell model, *AIAA J.* (2021) 1–14.
- [43] E. Carrera, M. Filippi, Vibration analysis of thin/thick, composites/metallic spinning cylindrical shells by refined beam models, *J. Vib. Acoust.* 137 (3) (2015).
- [44] A. Pagani, E. Carrera, Unified formulation of geometrically nonlinear refined beam theories, *Mech. Adv. Mater. Struct.* 25 (1) (2018) 15–31.
- [45] E. Carrera, M. Filippi, Variable kinematic one-dimensional finite elements for the analysis of rotors made of composite materials, *J. Eng. Gas Turbines Power* 136 (9) (2014).
- [46] M. Cinefra, C. Chinosi, L. Della Croce, MITC9 shell elements based on refined theories for the analysis of isotropic cylindrical structures, *Mech. Adv. Mater. Struct.* 20 (2) (2013) 91–100.
- [47] R.J. Allemang, The modal assurance criterion - twenty years of use and abuse, *Sound Vib.* 37 (8) (2003) 14–23.
- [48] M. Pastor, M. Binda, T. Harčarik, Modal assurance criterion, *Procedia Eng.* 48 (2012) 543–548.